

# Cation Molecular Structure Affects Mobility and Transport of Electrolytes in Porous Carbons

Naresh C. Osti<sup>1,\*</sup>, Boris Dyatkin<sup>2,§</sup>, Alejandro Gallegos<sup>3</sup>, David Voneshen<sup>4</sup>, Jong-Kahk Keum<sup>1</sup>, Ken Littrell<sup>1</sup>, Pengfei Zhang<sup>5</sup>, Sheng Dai<sup>5</sup>, Jianzhong Wu<sup>3</sup>, Yury Gogotsi<sup>2</sup>, Eugene Mamontov<sup>1,\*</sup>

<sup>1</sup>Neutron Scattering Division, Oak Ridge National Laboratory, Oak Ridge, Tennessee 37831, United States

<sup>2</sup>Department of Materials Science and Engineering and A. J. Drexel Nanomaterials Institute, Drexel University, Philadelphia, Pennsylvania 19104, United States

<sup>3</sup>Department of Chemical and Environmental Engineering, University of California – Riverside, Riverside, California 92521, United States

<sup>4</sup>ISIS Pulsed Neutron and Muon Source, STFC Rutherford Appleton Laboratory, Harwell Campus, Didcot, Oxfordshire OX11 0QX, United Kingdom

<sup>5</sup>Chemical Science Division, Oak Ridge National Laboratory, Oak Ridge, Tennessee 37831, United States

<sup>§</sup>Current address: U.S. Naval Research Laboratory, Washington, DC 20375, USA

\*Corresponding author: [ostinc@ornl.gov](mailto:ostinc@ornl.gov), [mamontove@ornl.gov](mailto:mamontove@ornl.gov)

## Abstract

We examined the electrosorption and ion dynamics of imidazolium-based room temperature ionic liquids (RTILs) having short (3-carbon, **C3mim<sup>+</sup>**) and long (12-carbon, **C12mim<sup>+</sup>**) cations, **that is, 1-propyl-3-methylimidazolium bis(trifluoromethylsulfonyl)imide (C3mimTFSI) and 1-dodecyl-3-methylimidazolium bis(trifluoromethylsulfonyl)imide (C12mimTFSI)**, confined in ordered mesoporous carbon (OMC) and analyzed the influence of **the cation alkyl chain length** on the ion dynamics and the capacitive behavior using electrochemical measurements together with quasi-elastic neutron scattering (QENS) observations and classical density functional theory (cDFT) computations. Electrochemical tests highlighted the significant influence of specific applied potentials on accumulated charge storage densities and on the limits of saturation of larger electrolytes in the pores. Computational analyses corroborated these findings and predicted a 16% increase in the capacitance of the smaller-cation electrolyte under high applied potentials. However, QENS experiments revealed a behavior of decoupling of alkyl chain dynamics from the ring in electrolytes with larger ions. cDFT calculations identified density

34 spikes for C12mim<sup>+</sup> away from the pore walls to further corroborate this unique behavior. Our  
35 insights into chain length-dependent dynamics and electrosorption in complex electrolyte-  
36 electrode systems deepen fundamental understanding of confined RTIL electrolyte behavior in  
37 the porous carbon electrodes.

## 38 **Introduction**

39 Solvent-free (neat) electrolytes offer significant advantages in electrochemical energy  
40 harvesting, conversion, and storage applications.<sup>1, 2</sup> These systems increase electrolyte stability  
41 across a wide range of temperatures and electric potentials. In turn, irreversible decomposition  
42 and breakdown of electrolyte is minimized.<sup>3, 4</sup> Room temperature ionic liquids (RTILs), which  
43 are poorly coordinated organic salts that dissociate into ions without the need for a secondary  
44 solvent, serve as electrolytes in RTIL-based supercapacitors. These systems are non-volatile,  
45 non-flammable, and much more electrochemically stable than conventional aqueous or organic  
46 electrolyte alternatives.<sup>5, 6</sup> Intuitively, resulting ion behaviors in pores are substantially different  
47 from traditional electric double layer (EDL) paradigms and, subsequently, are contingent on the  
48 ionic properties, their electrosorption dynamics, and interactions with electrode surfaces.<sup>7</sup>

49 In order for supercapacitors to efficiently charge and discharge, the electrode and electrolyte  
50 components require concomitant tuning and optimization. Intrinsic properties of both electrodes  
51 (pore architecture, surface chemistry) and electrolytes (ion dimensions, chemical composition)  
52 influence the overall device capacitance and rate handling.<sup>8-10</sup> In order to meet the demands for  
53 electrolytes that offer exceptional performance at high voltages (especially negligible vapor  
54 pressure, high ionic conductivity, and thermal stability), prior research efforts have yielded a  
55 broad variety of viable ionic liquids.<sup>11-13</sup> With respect to the electrode component, numerous  
56 porous materials<sup>9, 10, 14</sup> have been tailored in order to match corresponding electrolytes and

57 maximize charge storage and capacitance. A critical parameter that governs the electrochemical  
58 performance of EDLCs remains the quantity of accessible electrode pore surface on which ions  
59 can be electro-adsorbed. Carbon materials with internal surfaces<sup>15</sup> offer over 2,000 m<sup>2</sup> g<sup>-1</sup> of  
60 available electrode surface area for ion accumulation.<sup>16, 17</sup> However, important trade-offs  
61 between narrower pores (which densely pack ions) and wider pores (which allow efficient ion  
62 mobilities) are required for optimal electrode systems.<sup>18-21</sup> Consequently, careful analysis of  
63 essential properties of electrodes and electrolytes and balancing of desired attributes is required  
64 in order to maximize their performance capabilities of supercapacitors.

65 In order to assess essential fundamental behaviors that govern the performance of  
66 supercapacitors, we investigated electrodynamic and electrochemical performance of two RTILs,  
67 1-propyl-3-methylimidazolium bis(trifluoromethylsulfonyl)imide (C3mimTFSI) and 1-dodecyl-  
68 3-methylimidazolium bis(trifluoromethylsulfonyl)imide (C12mimTFSI, that incorporate  
69 identical imidazolium rings and anions that possess different alkyl chain lengths on each of their  
70 respective cations. Subsequently, such divergently sized electrolytes differ greatly in their ability  
71 to enter narrow pores, arrange in co-ion and counterion layers on charged surfaces, and shuffle  
72 past each other during dynamic potential conditions. We confined these electrolytes in ordered  
73 mesoporous carbon (OMC) that included both micropores and mesopores and, therefore, allowed  
74 insight into both tightly confined and relatively unrestricted electrolyte dynamics. We  
75 complemented empirical electrochemical measurements (in potentiodynamic conditions) and  
76 neutron scattering observations (in electrochemically neutral conditions) with computational  
77 analysis (classical density functional theory) in order to provide theoretical explanations.  
78 Electrochemical results highlighted the significance of the cation size on impedance and rate  
79 handling capabilities, while charge storage capacities further suggested a voltage-dependent

80 saturation limit for the larger electrolyte species. When we increased the cation alkyl chain  
81 length from 3 to 12, we noted a corresponding 16% capacitance decrease at high voltages. While  
82 electrochemical measurements involved intrinsic co-linked electrosorption of cations and anions,  
83 quasi-elastic neutron scattering (QENS) measurements focused on the cations. In particular, they  
84 revealed decoupling of the alkyl chain dynamics from the motions of the imidazolium ring that  
85 occurred in cations with larger alkyl chains. Our approach offers important insights into  
86 behaviors of charge carriers during electrosorption and, in place of dated conventional concepts,  
87 offers foundations for more accurate electric double layer models.

## 88 **Experimental**

89 Porosimetry: A Quadrasorb (Quantachrome Instruments, Boynton Beach, FL) Gas Sorption  
90 Analyzer was used to collect information regarding the specific surface area (SSA) and pore size  
91 distribution (PSD) of the original ordered mesoporous carbon (OMC) material. The OMC was  
92 synthesized following the established procedure.<sup>22</sup> The instrument collected isothermal  
93 measurements at 77 K (liquid N<sub>2</sub> coolant) with a nitrogen adsorbate in the 0.0075 – 0.995 P/P<sub>0</sub>  
94 relative pressure regime. The SSA was calculated using the Brunauer-Emmett-Teller (BET)  
95 equation for adsorption values collected in the 0.05 – 0.30 P/P<sub>0</sub> range<sup>23</sup>. The PSD was derived  
96 using Quenched Solid Density Functional Theory (QSDFT) analysis of the adsorption branch.<sup>24</sup>  
97 Quadrawin Software (Quantachrome Instruments) was used for all calculations. Ion dimensions  
98 were approximated from calculations of molecular models of the electrolyte species produced  
99 using the Molinspiration Cheminformatics 2018 software package  
100 (<http://www.molinspiration.com>).

101 Electrochemistry Measurements: Electrodes were prepared according to previously developed  
102 procedures<sup>25, 26</sup>. OMC particles were dispersed in ethanol and mixed together with a

103 polytetrafluoroethylene (PTFE) polymer binder in a 95:5 w/w ratio of carbon to polymer. The  
104 slurries were rolled into 100  $\mu\text{m}$  thick freestanding electrode films with a rolling mill, and a 13  
105 mm diameter hole punch subsequently excised identical circular electrodes out of the film sheet.  
106 Electrochemical cells were assembled inside an Ar-filled glovebox in symmetrical, two-electrode  
107 configurations. Cells used L-shaped carbon-coated aluminum current collectors, and 2 layers of  
108 3501 Celgard® separator were inserted between the electrodes. The specific ionic liquids soaked  
109 the separator sheets prior to experiment in order to introduce the electrolyte to the electrodes.

110 Electrochemical measurements included three different techniques<sup>27</sup>. Electrochemical  
111 impedance spectroscopy (EIS) measurements collected real and imaginary impedance by  
112 oscillating voltage (10 mV amplitude) centered on 0.0 V vs. OCP with a dampening oscillation  
113 in the 200 kHz – 10 mHz frequency range. Cyclic voltammetry (CV) sweeps were carried out at  
114 varying sweep rates between 0.5  $\text{mV s}^{-1}$  and 1000  $\text{mV s}^{-1}$  in the 0  $\leftrightarrow$  +2.5 V window (net  
115 potential difference between the two electrodes). Gravimetric capacitance ( $C_{sp}$ ) was calculated  
116 according to the following equation:

$$117 \quad C_{sp} = 2 \int_{V_0}^{V_f} \frac{I}{\frac{dV}{dt} m_E V_w} dV \quad (1)$$

118 The equation uses  $V_0$  as the initial potential (fixed at zero) and  $V_f$  as the vertex potentials;  $m_E$  as  
119 the mass of a single electrode;  $V_w$  is the electrochemical potential window (2.5 V); and  $\frac{dV}{dt}$  is the  
120 sweep rate<sup>27</sup>. Square wave chronoamperometry (SWC) applied instantaneous 1.0 V, 2.0 V, and  
121 2.5 V potential differences across the cell. SWC recorded time-resolved current during 60  
122 minutes of steady-state potential conditions and subsequently derived total accumulated charge  
123 for each measurement.

124 Classical Density Functional Theory (cDFT) Calculations: The computational approach adopted  
125 a coarse-grained model that represented imidazoles with positively charged spheres that were

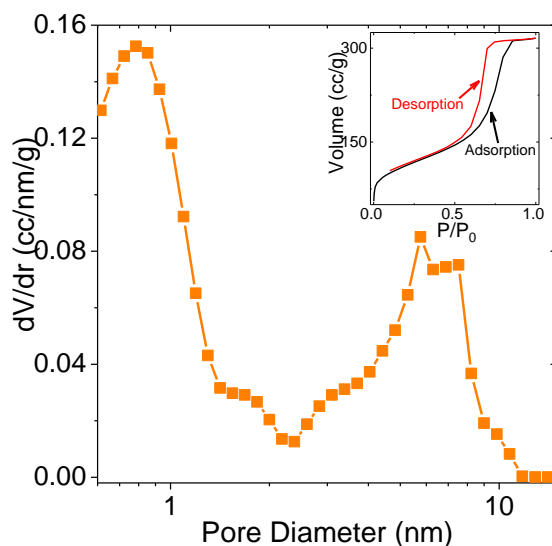
126 tangentially connected to a chain of neutral spheres. Therefore, each neutral sphere amounted to  
127 a propyl (3-carbon) group. Single negatively charged spheres represented the TFSI anions. Prior  
128 to the analyses by Ye and Shreeve yielded estimated sphere dimensions and densities of ionic  
129 liquids.<sup>28</sup> A slit pore model with a fixed wall surface potential represented pores and exhibited  
130 dimensions that matched the porosity of the experimental OMC material. The theoretical details  
131 and a schematic (Fig. S1) of this model is given in Supplementary Information.

132 Quasi-elastic Neutron Scattering (QENS): OMC powders, synthesized as reported,<sup>22</sup> were  
133 infiltrated with the three electrolytes according to the previously reported procedure.<sup>29</sup>  
134 C3mimTFSI and C12mimTFSI fully filled the volume of OMC pores of specific powder  
135 quantities (the SI section on the QENS measurements that describes the pore filling method).  
136 Small angle neutron scattering (SANS) profiles (Fig. S3) of empty and the ionic liquids  
137 (C3mimTFSI and C12mimTFSI) filled OMC show that the ionic liquids are present inside the  
138 pores (see SI for SANS details). QENS studies were carried out on the cold neutron multi-  
139 chopper spectrometer (LET)<sup>30</sup> in Oxfordshire, UK that was operated in repetition rate  
140 multiplication mode.<sup>31</sup> These capabilities of the LET allow data collection at several incident  
141 wavelengths to probe the dynamics which span different time scales. We performed an  
142 experiment at the LET using four incident energies (560, 860, 1340 and 2500  $\mu\text{eV}$ ), which  
143 yielded the data sets with the following energy resolutions (full width at half-maximum,  
144 FWHM): 3.95, 8.43, 18.2 and 44.0  $\mu\text{eV}$ , with the corresponding momentum transfer (Q-  
145 coverage) of [0.3-0.7], [0.3-1.0], [0.3-1.4] and [0.3-1.85]  $\text{\AA}^{-1}$ . QENS spectra were measured at  
146 300 K from  $[\text{C}_n\text{mim}^+][\text{TFSI}]$  with a carbon chain length  $n= 3$  and 12 confined in OMC of  
147 average pore size of 7.3 nm. Sample-specific resolution spectra were measured at 5 K. Desired

148 sample temperatures was maintained using closed cycle refrigerator (CCR). Data were reduced  
149 and analyzed by Mantid<sup>32</sup> and DAVE<sup>33</sup> software, respectively.

## 150 Results and Discussion

151 The pore size distribution for ordered mesoporous carbon is shown in Figure 1. Its isotherm  
152 (shown in the inset) exhibited typical Type IV behavior with pronounced hysteresis, suggesting a  
153 significant contribution of mesopores to the total porosity<sup>34</sup>. Nitrogen adsorption analysis  
154 indicated that the specific surface area (SSA) of the carbon material was  $390 \text{ m}^2 \text{ g}^{-1}$ , and the total  
155 pore volume was  $0.47 \text{ cm}^3 \text{ g}^{-1}$ . While the material exhibited some micropores (0.79 nm was the  
156 most predominant diameter), this narrow pore range contributed less than 25 % of the cumulative  
157 accessible surface. The pore structure was mostly comprised of mesopores.



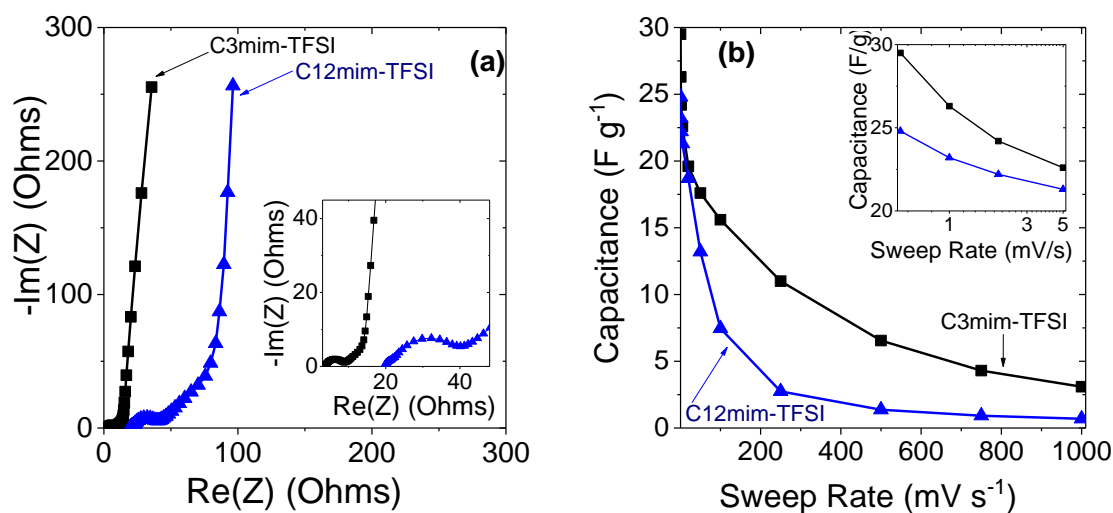
158 **Figure 1.** Semilogarithmic plot of pore size distribution for the ordered mesoporous carbon (OMC) studied  
159 in this work. Inset includes the nitrogen sorption/desorption isotherms.

161 The electrode material's mesopores (2.0 nm – 10.0 nm predominant pore diameter range  
162 for OMC, 7.3 nm most commonly occurring slit width) could accommodate all ion species of  
163 both electrolytes without limiting their individual translational and rotational motion. The  
164 dimension of the  $\text{C3mim}^+$  cation and  $\text{TFSI}^-$  anion were remarkably similar (respectively, 1.03 nm  
165 and 1.10 nm lengths; 0.65 nm and 0.5 nm widths; and  $0.14 \text{ nm}^3$  and  $0.15 \text{ nm}^3$  molecular

166 volumes). Furthermore, all three ions were able to rotate freely among two axes in the  
167 micropores. However, the C12mim<sup>+</sup> cation's larger size (2.18 nm width and 0.29 nm<sup>3</sup> volume)  
168 significantly inhibited its ability to rotate along all three axes in the 0.78 nm wide micropores.  
169 Subsequently, for C12mimTFSI, ion sieving limitations and resulting impedance were expected  
170 to negatively impact electrosorption rates and charge accumulation capabilities into smaller  
171 pores. Although the mesopores constituted a greater fraction of the entire pore architecture, and  
172 thus accounted for most of the observed charge storage behavior and electrolyte dynamics,  
173 "electrowetting" of smaller pores became an important factor that affected experimental  
174 supercapacitor performance in higher-voltage regimes.

175 Electrochemical tests of the two electrolytes showed distinct capacitance and  
176 electrodynamic differences between the two electrolytes in this micro- and meso-porous carbon  
177 system. From a mobility perspective, the Nyquist plot in Figure 2 (a) shows the dynamics of  
178 C3mimTFSI and C12mimTFSI in OMC pores under a rapidly fluctuating potential. As expected,  
179 the C3mimTFSI electrolyte exhibits greater ionic mobility and lower ionic impedance for the  
180 entire frequency range. The equivalent series resistance (ESR), as determined by  $\text{Re}(Z)$  at  $-\text{Im}(Z)$   
181  $= 0^{35}$ , was 3.7  $\Omega$  for C3mimTFSI and 19.7  $\Omega$  for C12mimTFSI. The charge transfer resistance  
182 (semi-circular region) was, similarly, much larger for the electrolyte with a longer chain length  
183 for the cation. The "knee frequency" time constant for C3mimTFSI was 4.7 s while that for  
184 C12mimTFSI is 28.8 s. Even low-frequency behavior featured relatively greater impedance for  
185 the C12mimTFSI electrolyte: its impedance angle (Phase (Z)) was -69 ° at 10 mHz, whereas  
186 C3mimTFSI was much more capacitive at the same frequency (Phase (Z) = -82 °). **The**  
187 **impedance behavior suggests that the large alkyl chain on the C12mim<sup>+</sup> cation of C12mimTFSI**  
188 **imposed noticeable mobility limitations on both short-range, rapid interactions and long-range,**

189 extended time-scale processes. In the case of the former (rapid co-ion/counterion exchange at  
 190 electrode/electrolyte interfaces during high-frequency voltage fluctuations), the relative sluggish  
 191 process and slow motion of the large cations with respect to the anions imposes detrimental  
 192 effects on current flow through electrodes of C12mimTFSI system. These effects translate into  
 193 higher equivalent series and charge transfer resistance values observed for the electrolyte with  
 194 larger chain lengths on the cation. Furthermore, at longer time scales (that account for long-range  
 195 diffusion of ions through the bulk electrode across the entire ultracapacitor), relative mobilities  
 196 of larger C12mim<sup>+</sup> cations limit the resulting charge/discharge rates. Consequently, impedance-  
 197 induced ionic resistance precludes the entire C12mimTFSI system from behaving as an ideal  
 198 capacitor at near-static states. The impedance results for these charge storage systems, which  
 199 used the same anions for both electrolytes, reinforced the concept that co-ion and counterion  
 200 mobilities are intertwined.

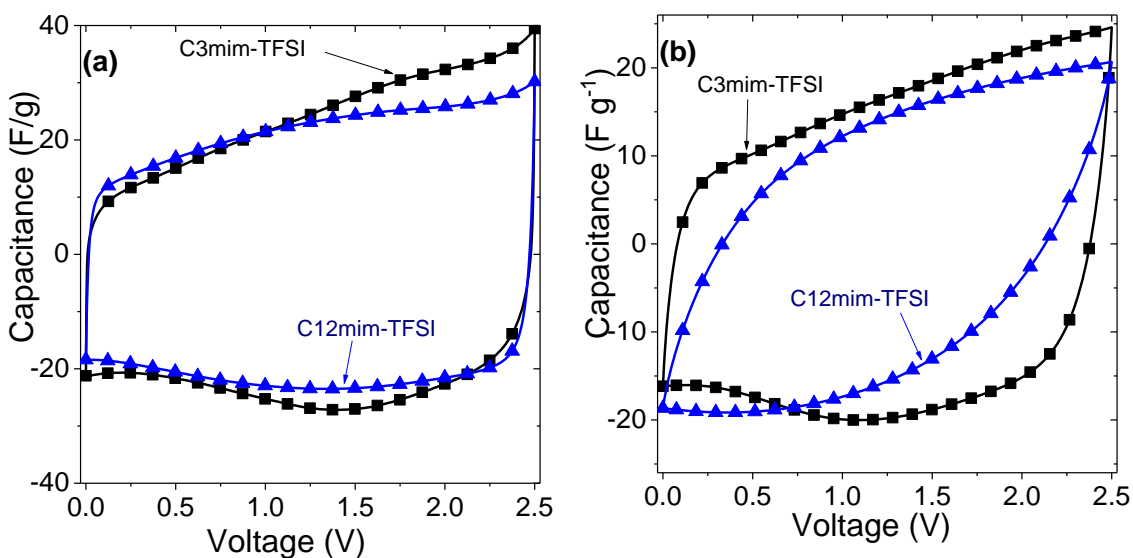


201 **Figure 2.** (a) The Nyquist plot compares the electrochemical impedance of C3mimTFSI and  
 202 C12mimTFSI in ordered mesoporous carbon. Inset zooms in the high-frequency region. (b) Plot of rate  
 203 handling comparison for the two electrolytes as from cyclic voltammetry scans in the 0.2 – 1000 mV/s  
 204 sweep range.  
 205  
 206

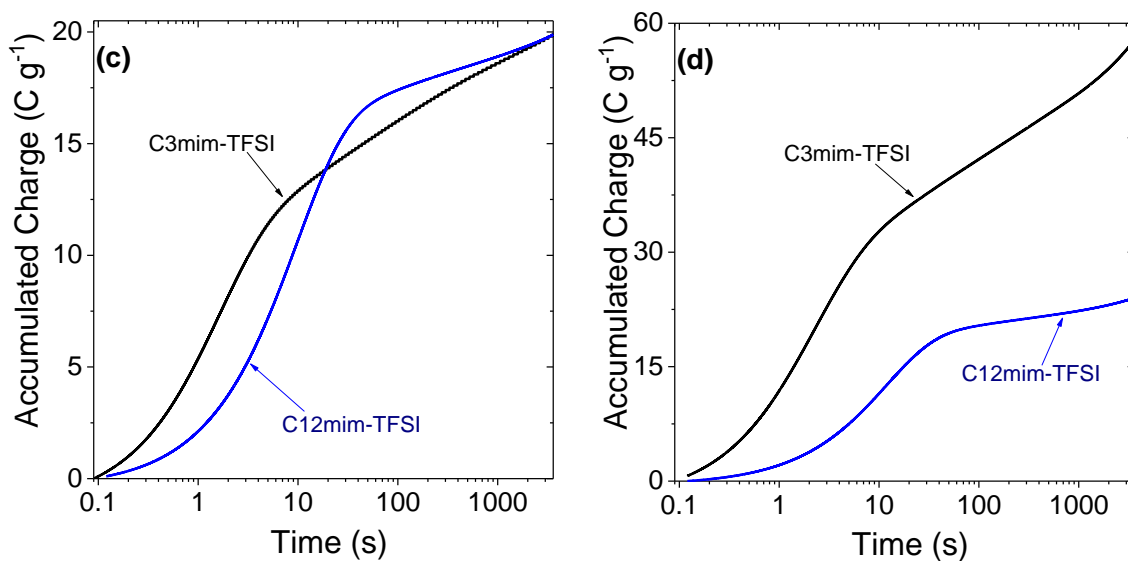
207 Results of CV capacitance calculations over the entire 0.5 – 1000 mV s<sup>-1</sup> sweep range are  
208 shown in Figure 2 (b). In behavior that parallels the EIS results, C3mimTFSI showcased higher  
209 capacitance than C12mimTFSI throughout the entire scan rate range. As expected, C3mimTFSI  
210 benefited from the enhanced electrolyte dynamics and retained more capacitance at higher  
211 charge/discharge rates ( $\geq 20$  mV s<sup>-1</sup>). However, these differences were not significant at low  
212 sweep rates ( $\leq 5$  mV s<sup>-1</sup>). In fact, in that range, C3mimTFSI's rate handling decayed by 23%,  
213 while C12mimTFSI decayed by only 14%. **Conversely, in the 20 mV/s – 1000 mV/s,**  
214 **C3mimTFSI experiences a capacitance decay of 84%, while C12mimTFSI's capacitance decays**  
215 **by over 96% over the same sweep range.**

216 Specific voltammograms at different sweep rates provide more insight into this observation.  
217 Figure 3 (a) shows the CV sweeps at 2 mV s<sup>-1</sup>. At this low charge/discharge rate, both data sets  
218 maintained relatively similar rectangular shapes, and ionic impedance did not drastically  
219 interfere with electrosorption at low voltages. The low-voltage plots segment shows greater rates  
220 of charge accumulation for C12mimTFSI up to 1.0 V. However, past that threshold, capacitance  
221 of C3mimTFSI increased, whereas capacitance of C12mimTFSI plateaued. During the discharge  
222 process, the C3mimTFSI system showed some evidence of ion **saturation** (a “butterfly” shape) at  
223 low voltages<sup>36</sup>; this behavior was absent for the electrolyte with the larger cation chain length.  
224 At higher rates (50 mV s<sup>-1</sup>, Figure 3 (b)), this **charge saturation** behavior was still present for  
225 C3mimTFSI. However, this rapid charge/discharge rate enhanced the ionic resistance and  
226 induced significant deviations of the C12mimTFSI system from its ideal rectangular CV curve.  
227 These takeaways suggest that, while both electrolytes electrosorb into mesopores with relative  
228 similar ease, narrower micropores (Fig. 1) exclude C12mimTFSI and limit its capacitance.  
229 Recent results in a bimodal porous carbon system exhibited similar findings.<sup>17</sup> **The overall trends**

230 of cyclic voltammogram results paralleled those of impedance measurement results: lower  
231 mobility of C12mim<sup>+</sup> increases its resistance and, as compared to C3mim<sup>+</sup>, lowers its  
232 capacitance and rate handling ability. The relative time scales affect the extent to which these  
233 observations parallel each other. At low impedance oscillation frequencies (and corresponding  
234 low sweep rates), the phase angle measurements and capacitance values deviate only slightly.  
235 However, the fivefold higher series resistance at high oscillation rates parallels the significant  
236 capacitance decay of the C12mimTFSI system.



237

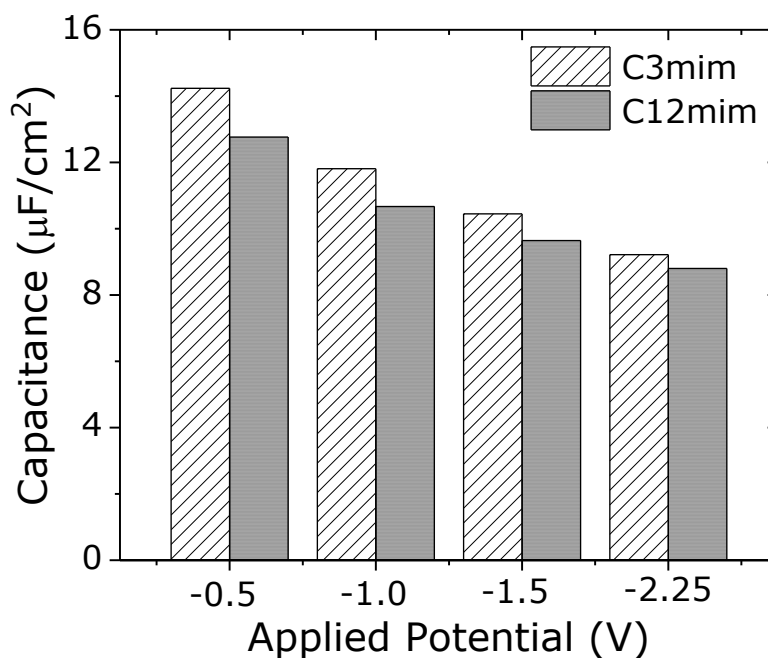


238

239 **Figure 3.** (A) Cyclic voltammetry in the 0 – 2.5 V window at 2 mV/s rate. (B) Cyclic voltammetry at a 50  
240 mV/s sweep rate. (C) Square-wave chronoamperometry comparison of charging of C3mimTFSI and  
241 C12mimTFSI up to 1.0 V. (D) Square-wave step charging up to 2.0 V. C, D are semilogarithmic plots.

242  
243 Square wave chronoamperometry shown in Figure 3 (c) delves more deeply into the  
244 processes that occur at each voltage. Steady-state charging up to 1.0 V results in the same charge  
245 accumulation for both electrolytes. This finding parallels the results from slow sweep rates  
246 shown for CVs. However, at 2.0 V, C3mimTFSI collects a significantly greater amount of charge  
247 than C12mimTFSI (Figure 3 (d)). This behavior, likewise, corroborates the cyclic  
248 voltammogram sweeps in the higher voltage region. The dynamic and static electrochemical tests  
249 suggest that the alkyl chain length influences ion saturation and filling of pores<sup>37</sup>, and that this  
250 process primarily depends on the specific applied potential of the system<sup>38</sup>. Furthermore, since  
251 the pore structure includes micropores and mesopores, “electrowetting” of small pores may only  
252 occur under higher applied potentials<sup>39</sup>. Since C12mim<sup>+</sup> has greater dimensional limitations than  
253 C3mim<sup>+</sup>, only the latter may take advantage of micropores and increase capacitance at higher  
254 voltages.

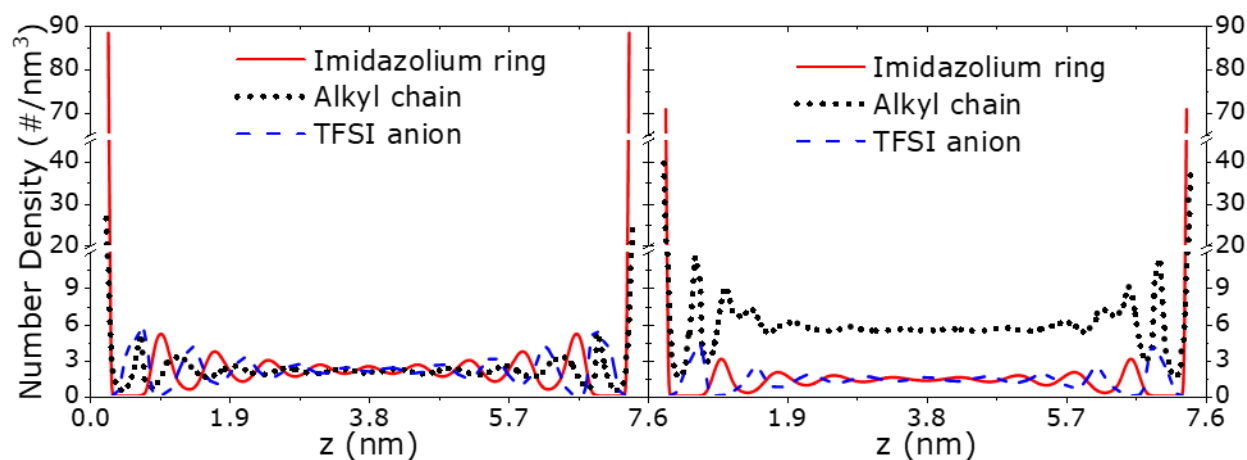
255 From the aforementioned experiments, we note distinct behaviors that stem from the  
256 electrode material’s dominant micropore region and mesopore region. **From square wave**  
257 **chronoamperometry measurements, we find that capacitance capability of C12mimTFSI underperforms**  
258 **that of C3mimTFSI by ~16% at a high voltage.** However, in-depth voltage-dependent analysis and  
259 data refinement show that C3mimTFSI and C12mimTFSI mirror each other’s performance until  
260 the potential exceeds -1.0 V vs. OCP. Beyond this threshold, the capacitance for C12mimTFSI  
261 changes only slightly while C3mimTFSI’s charge accumulation continues to rise with voltage.  
262 Therefore, we conclude that there must be a substantial change in the fundamental charging and  
263 ion arrangement under applied voltages greater than -1.0 V vs. OCP that leads to this trend.



264  
 265 **Figure 4.** Comparison of computed cDFT capacitance with applied potential for the ionic liquids  
 266 C3mimTFSI and C12mimTFSI confined in a mesopore (7.6 nm).

267 To complement electrochemical experimental results, we performed cDFT calculations to  
 268 provide insights into the structure and properties of the EDL for this system. We approximated  
 269 the mesopore pore size to be equal to 7.6 nm for subsequent calculations. For the cDFT  
 270 calculations, we chose to examine the negative electrode only as we found that the positive  
 271 electrode showed only minor changes with cation specie (not shown here). Here, applied  
 272 potential refers to the potential on an individual electrode and the difference between the positive  
 273 and negative electrode is the cell voltage. The computed capacitance versus applied potential  
 274 (Figure 4) for the studied system shows that the capacitance is lower for C12mimTFSI relative to  
 275 C3mimTFSI and, at -1.0 V, the capacitance is lower by 10%. The density profiles in Figure 5  
 276 provide further insight into the reduced capacitance of C12mimTFSI relative to C3mimTFSI.  
 277 Although the number density profiles between the two ionic liquids are similar, there is a  
 278 noticeable decrease in the contact density of the cation and the oscillation of the EDL structure

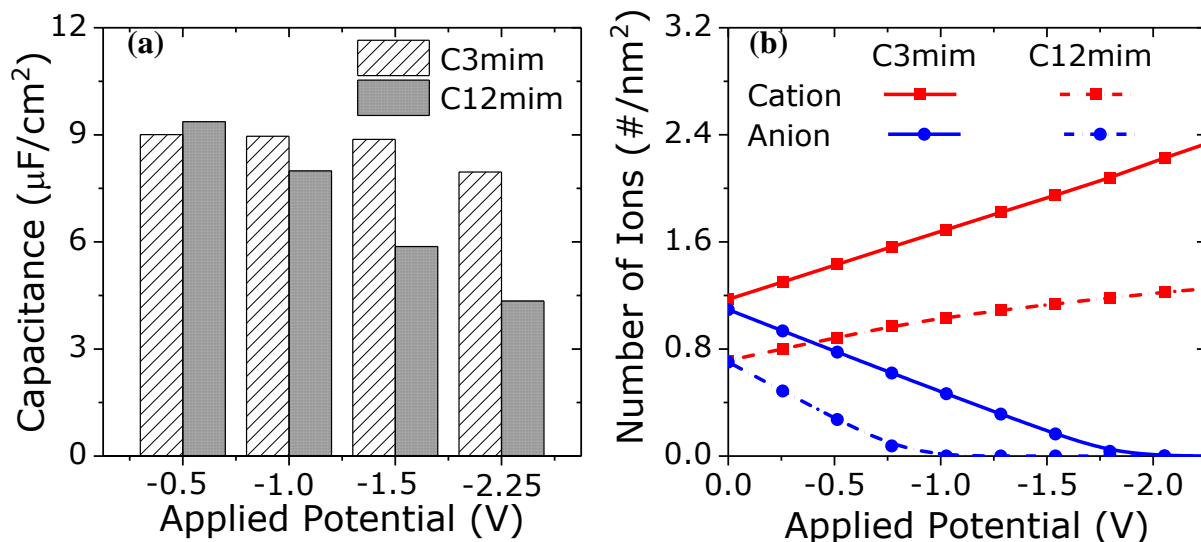
279 when the alkyl chain length is increased. This results in a less packed EDL structure and  
280 provides more freedom for the alkyl chain which tends to spread away from the wall. As a result,  
281 there is a lower net charge accumulation in the pore that leads to a lower capacitance. Note that  
282 comparatively smaller space to engage in the chain motions is available for the cation chains in  
283 the smaller mesopores, where the ions occupy the space only near the walls, as demonstrated by  
284 the density profiles (Fig. S2) of the ions in 2.6 nm pores.



285  
286 **Figure 5.** The number density profiles for C3mimTFSI (left panel) and C12mimTFSI (right panel)  
287 confined in a mesopore (7.6 nm) with an applied surface potential of -1.0 V.

288 Insight provided by the mesopore calculation, however, fails to provide a reason for why  
289 the electrochemical results show a potential at which the C12mim charge accumulation is greatly  
290 hindered. To understand this, we focused on the material's microporous region by performing  
291 cDFT calculations with a pore size of 0.70 nm. We found that this region correctly matches the  
292 observed capacitance plateau for C12mimTFSI (shown in Figure 6a). To understand this  
293 plateau, we plot the number of ions with respect to the applied potential in Figure 6b. Here it  
294 becomes clear that the micropore is filled with only cations at -1.0 V, and further negative  
295 increase in applied potential results in a smaller increase in cations relative to when there were  
296 anions present. The lower negative potential threshold for anion depletion for C12mimTFSI

297 compared to C3mimTFSI can be explained by the alkyl chain effectively displacing the anions  
 298 from the micropore. As a result, the charge accumulation is much lower for C12mimTFSI than  
 299 for C3mimTFSI past this potential threshold and explains the electrochemical results.



300  
 301 **Figure 6.** The capacitance at different applied potentials (a) and the number of ions present at  
 302 different applied potentials (b) for C3mimTFSI and C12mimTFSI in a micropore (0.7 nm).

303 We employed QENS technique to study the microscopic dynamics of C3mimTFSI and  
 304 C12mimTFSI confined in OMC. QENS has been a technique of choice to probe the dynamics of  
 305 confined fluids.<sup>40-42</sup> Since hydrogen has very high neutron incoherent scattering cross-section<sup>43</sup>,  
 306 the hydrogen atoms present in the cation of the RTILs dominates the QENS signal. Dynamic  
 307 susceptibility (Fig. S4) derived from QENS spectra reveals a localized, non-Debye-like  
 308 dynamics in both systems. Therefore, a Cole-Cole distribution function<sup>44</sup> was used to analyze the  
 309 QENS data (see SI for details). Representative spectra together with a Cole-Cole model fits are  
 310 presented in Figure S5 in Supplementary Information. Figure 7 (a and b) shows a Q dependence  
 311 of the HWHM of the QENS signal for both C3mimTFSI and C12mimTFSI measured with  
 312 different incident neutron energies used. The values of HWHM tend to be somewhat higher for  
 313 C12mimTFSI (Fig 7b) compared to those for C3mimTFSI (Fig. 7a). This is unexpected, because

314 higher HWHM values obtained for C12mimTFSI confined in OMC suggest higher detected  
315 mobility of C12mim<sup>+</sup> ions, that are larger than C3mim<sup>+</sup> ions, which would be counterintuitive. It  
316 has already been shown that the dynamics of cations becomes significantly reduced when the  
317 size of the cations increases.<sup>45</sup> Therefore, C12mim<sup>+</sup> is expected to exhibit slower mobility.  
318 However, we note that the dependence of the HWHM in Figure 7 (a and b) is not quadratic with  
319 Q, as one would expect for translational diffusion of ions, thus suggesting that we are not  
320 probing the diffusivity of the entire cations. Instead, the QENS measurement is exploring the  
321 local mobility of the alkyl chains of the cations. This is further evidenced by the low values of  
322 the power law exponent (see SI for scaling of structural relaxation time).

323 Overall, there is not a strong dependence of  $\langle\tau\rangle$  (which is inversely proportional to the  
324 HWHM) with Q. However, a clear crossover is present at  $Q = 0.7 \text{ \AA}^{-1}$ , which is equivalent to a  
325 length scale of  $\sim 9 \text{ \AA}$ . Because this length scale approximately corresponds to the size of the  
326 OMC micropores as presented in Figure 1, it would be tempting to associate the data above and  
327 below the crossover with the cation dynamics in the micro- and meso-pores, respectively.  
328 However, it is unlikely that the cation dynamics in the mesopores could be more spatially  
329 restricted, with a weaker Q-dependence than that in the micropores. Instead, the mobility probed  
330 in the QENS experiment is associated with the side chains of the cations, exploring the localized  
331 volume near the cation. The localized motions of this type are known to exhibit a crossover in  
332 the Q-dependence of their HWHM at the length scale corresponding to the characteristic size of  
333 the effective localized volume inside which the motion takes place.<sup>43</sup>

334

335

336

337

338

339

340

341

342

343

344

345

346

347

348

349

350

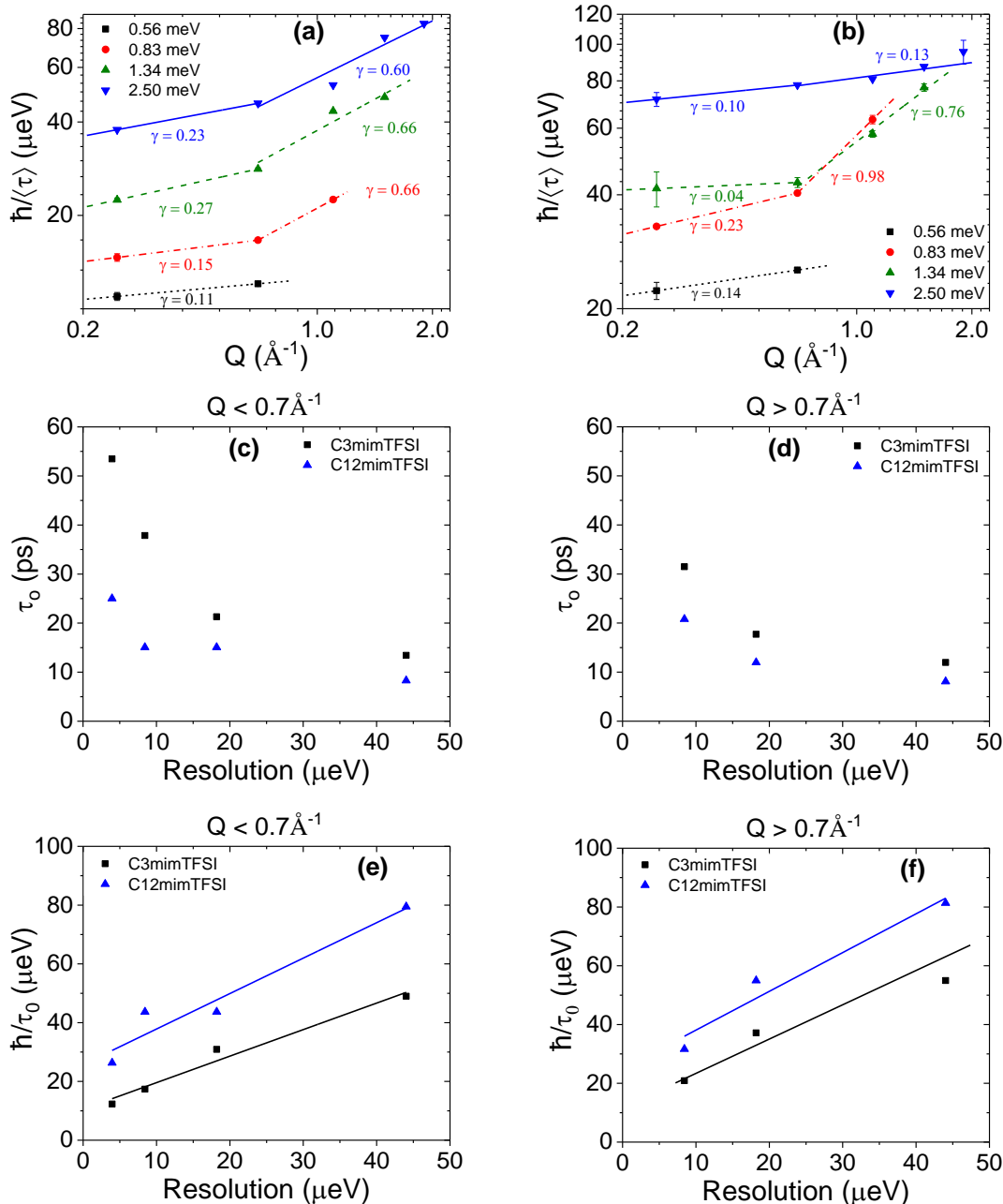
351

352

353

354

355



356 **Figure 7.** Q dependence of the QENS signal HWHM (a) C3mimTFSI (b) C12mimTFSI, showing a  
 357 crossover at  $\sim Q = 0.7 \text{\AA}^{-1}$ , where  $\gamma$  is the corresponding slope of the lines. Calculated structural relaxation  
 358 time,  $\tau_0$ , in the two Q regimes (c) and (d) with the corresponding Q-averaged QENS broadening (e) and  
 359 (f). The values are plotted as a function of the instrument resolutions associated with the varied incident  
 360 neutron energies used in the QENS measurement.

361 This higher value of HWHM from C12mimTFSI also implies that, when the length of the side

362 chain attached to the imidazole ring increases, its mobility decouples from the mobility of the

363 ring. The long-range diffusivity of the cation, as whole, decreases with the cation size, yet the  
364 longer chains exhibit greater localized mobility. This is consistent with the density spikes  
365 observed in cDFT calculation for C12mim<sup>+</sup> away from the pore walls in Figure 5, where the  
366 chain is less affected by the interaction between the ions with the wall of the pores. In  
367 C3mimTFSI, the chain is shorter, and its mobility couples with that of the imidazole ring,  
368 resulting in the relatively lower chain's mobility compared to the chain in C12mimTFSI.

369 While the data in Figure 7 provide information on the Q-dependence and, thus, the  
370 geometry effects on the cation motions, the quantitative information on the time scale of the  
371 cation motions needs to be extracted from the parameter  $\tau_0$ , the structural relaxation time,  
372 obtained from the  $\langle\tau\rangle = \tau_0 Q^{-\gamma}$  relationship. In Figure 7 (c-f), this parameter is plotted for  
373 C3mimTFSI and C12mimTFSI as a function of the instrument resolution that varies with the  
374 incident neutron energy. In agreement with the data in Figure 7(a-b), C3mim<sup>+</sup> ions exhibit  
375 relatively longer structural relaxation times, that is, slower dynamics, compared to C12mim<sup>+</sup> ions  
376 (Figure 7 (c-d)). Shorter structural relaxation time for the larger C12mim<sup>+</sup> ions is an indication of  
377 the dynamic decoupling between the main ring and the side chain, similar to the dynamic  
378 decoupling observed in an ionic liquid with octyl side chain.<sup>46</sup> While the longer chains of the  
379 C12mim<sup>+</sup> exhibit enhanced localized mobility, the electrochemical performance is directly  
380 influenced by the mobility of cations as a whole, and the larger size of C12mim<sup>+</sup> results in a  
381 smaller capacitance compared to that of C3mim<sup>+</sup>.

382 The inverse of the structural relaxation time, corresponding to the QENS broadening  
383 effectively averaged over all Q values, shows approximately linear dependence with the  
384 instrument resolution (Figure 7 (e-f), bottom panels). This again suggests that the motions probed  
385 in the current QENS measurement are not related to the long-range translational diffusion of

386 cations as a whole, which is characterized by a well-defined diffusivity value and is thus  
387 expected to be resolution-independent. Instead, the QENS measurements probe a broad range of  
388 motions associated with the localized mobility of the alkyl chains of the cations, as already  
389 evidenced by the resolution-dependent shift of the low-energy peak in the susceptibility plots in  
390 Figure S4. The susceptibility plots in Figure S4 are essentially the model-independent raw data  
391 demonstrating that the measured characteristic relaxation time is indeed resolution-dependent.  
392 Depending on the energy resolution, the broadly distributed in time chain motions are weighed  
393 differently, thus giving rise to different average relaxation times. Decoupling of the chain from  
394 the imidazolium ring may help ion exchange at the electrode/electrolyte interface and  
395 compensate somewhat for its larger size, but that effect is hard to measure at this time and will  
396 need to be investigated in the future.

## 397 **Summary**

398 A combination of electrochemical measurements with QENS and cDFT allowed  
399 identification of the fundamental reasons behind differences in dynamics, electrosorption rates,  
400 and charge accumulation densities that occur when ionic liquid electrolytes with different cation  
401 alkyl chains are confined inside mesoporous carbon. Our combinational approach probed the  
402 influence of the electrolyte structure (alkyl chain length) on the charging behavior, arrangement,  
403 and dynamics of ions, and the corresponding changes in energy and power densities of  
404 supercapacitors. Although the takeaway with respect to the dynamics – C3mim is smaller and  
405 likely exhibits greater mobility than C12mim – appears intuitive, neutron scattering allowed us to  
406 probe the mobilities of individual components and added greater depth to the underlying  
407 mechanisms that ordinary electrochemistry measurements cannot capture. Specifically, our  
408 approach suggested that sufficiently long alkyl chains on cations begin to undulate and move

409 independently of the imidazolium ring. This observation was further supported by the high-  
410 density peaks, observed away from the pore walls, for the ionic liquid cation bearing longer alkyl  
411 chain, i.e., C12mimTFSI. Such behavior has never been observed before for confined  
412 electrolytes. This type of dynamic decoupling may benefit ion exchange phenomena at fluid-  
413 solid interface of energy storages devices and demands more rigorous research in the future.  
414 Furthermore, while larger ion size was also expected to reduce overall capacitance, our  
415 computational approach found the reasons why this decline is contingent on the specific applied  
416 voltage. In particular, past a critical -1.00 V threshold, cation concentration of the C12mimTFSI  
417 system becomes depleted in pores, and capacitance of the larger ion system becomes lower than  
418 that of the C3mimTFSI by 16%. These complex mechanisms, which cannot be captured by  
419 traditional testing and characterization techniques, are essential for future electrode and  
420 electrolyte design.

## 421 **Acknowledgements**

422 This work was supported as part of the Fluid Interface Reactions, Structures and Transport  
423 (FIRST) Center, an Energy Frontier Research Center funded by the U.S. Department of Energy,  
424 Office of Science, Office of Basic Energy Sciences. Work at ORNL's Spallation Neutron Source  
425 was sponsored by the Scientific User Facilities Division, Office of Basic Energy Sciences, U.S.  
426 Department of Energy. Oak Ridge National Laboratory is managed by UT-Battelle, LLC, for  
427 U.S. DOE under Contract No. DEAC05-00OR22725. Experiments at the ISIS Neutron and  
428 Muon Source were supported by a beamtime allocation (RB1520027) from the Science and  
429 Technology Facilities Council. This work is also supported by the National Science Foundation  
430 Graduate Research Fellowship under Grant No. DGE-1326120.

## 431 **References**

432 1. J. Kallhoff, G. G. Eshetu, D. Bresser, and S. Passerini, *ChemSusChem* **8**(13), 2154 (2015).  
433 2. U. A. Rana, M. Forsyth, D. R. MacFarlane, and J. M. Pringle, *Electrochimica Acta* **84**, 213  
434 (2012).  
435 3. D. R. Macfarlane, M. Forsyth, P. C. Howlett, J. M. Pringle, J. Sun, G. Annat, W. Neil, and E.  
436 I. Izgorodina, *Accounts of Chemical Research* **40**(11), 1165 (2007).  
437 4. D. R. MacFarlane, N. Tachikawa, M. Forsyth, J. M. Pringle, P. C. Howlett, G. D. Elliott, J. H.  
438 Davis, M. Watanabe, P. Simon, and C. A. Angell, *Energy & Environmental Science* **7**(1), 232  
439 (2014).  
440 5. M. Galinski, A. Lewandowski, and I. Stepniak, *Electrochimica Acta* **51**(26), 5567 (2006).  
441 6. M. Watanabe, M. L. Thomas, S. G. Zhang, K. Ueno, T. Yasuda, and K. Dokko, *Chemical*  
442 *Reviews* **117**(10), 7190 (2017).  
443 7. J. Vatamanu, Z. Z. Hu, D. Bedrov, C. Perez, and Y. Gogotsi, *Journal of Physical Chemistry*  
444 *Letters* **4**(17), 2829 (2013).  
445 8. T. Chen, and L. M. Dai, *Materials Today* **16**(7-8), 272 (2013).  
446 9. G. P. Wang, L. Zhang, and J. J. Zhang, *Chemical Society Reviews* **41**(2), 797 (2012).  
447 10. P. Simon, and Y. Gogotsi, *Nature Materials* **7**(11), 845 (2008).  
448 11. Q. W. Yang, Z. Q. Zhang, X. G. Sun, Y. S. Hu, H. B. Xing, and S. Dai, *Chemical Society*  
449 *Reviews* **47**(6), 2020 (2018).  
450 12. M. Beidaghi, and Y. Gogotsi, *Energy & Environmental Science* **7**(3), 867 (2014).  
451 13. V. L. Martins, and R. M. Torresi, *Current Opinion in Electrochemistry* **9**, 26 (2018).  
452 14. A. Vlad, and A. Balducci, *Nature Materials* **16**(2), 161 (2017).  
453 15. X. L. Chen, R. Paul, and L. M. Dai, *National Science Review* **4**(3), 453 (2017).  
454 16. R. Lin, P. Huang, J. Segalini, C. Largeot, P. L. Taberna, J. Chmiola, Y. Gogotsi, and P.  
455 Simon, *Electrochimica Acta* **54**(27), 7025 (2009).  
456 17. B. Dyatkin, N. C. Osti, Y. Zhang, H.-W. Wang, E. Mamontov, W. T. Heller, P. Zhang, G.  
457 Rother, P. T. Cummings, D. J. Wesolowski, and Y. Gogotsi, *Carbon* **129**, 104 (2018).  
458 18. N. Jackel, P. Simon, Y. Gogotsi, and V. Presser, *ACS Energy Letters* **1**(6), 1262 (2016).  
459 19. Y. He, R. Qiao, J. Vatamanu, O. Borodin, D. Bedrov, J. Huang, and B. G. Sumpter, *J*  
460 *Physical Chemistry Letters* **7**(1), 36 (2016).  
461 20. R. Futamura, T. Iiyama, Y. Takasaki, Y. Gogotsi, M. J. Biggs, M. Salanne, J. Segalini, P.  
462 Simon, and K. Kaneko, *Nature Materials* **16**(12), 1225 (2017).  
463 21. E. Eustache, C. Douard, A. Demortiere, V. De Andrade, M. Brachet, J. Le Bideau, T.  
464 Brousse, and C. Lethien, *Advanced Materials Technologies* **2**(10), 17001126 (2017).  
465 22. C. D. Liang, and S. Dai, *Journal of the American Chemical Society* **128**(16), 5316 (2006).  
466 23. S. Brunauer, P. H. Emmett, and E. Teller, *Journal of the American Chemical Society* **60**(2),  
467 309 (1938).  
468 24. G. Y. Gor, M. Thommes, K. A. Cychosz, and A. V. Neimark, *Carbon* **50**(4), 1583 (2012).  
469 25. B. Dyatkin, V. Presser, M. Heon, M. R. Lukatskaya, M. Beidaghi, and Y. Gogotsi,  
470 *ChemSusChem* **6**(12), 2269 (2013).  
471 26. C. R. Perez, S. H. Yeon, J. Segalini, V. Presser, P. L. Taberna, P. Simon, and Y. Gogotsi,  
472 *Advanced Functional Materials* **23**(8), 1081 (2013).  
473 27. M. D. Stoller, and R. S. Ruoff, *Energy & Environmental Science* **3**, 1294 (2010).  
474 28. C. F. Ye, and J. M. Shreeve, *Journal of Physical Chemistry A* **111**(8), 1456 (2007).  
475 29. B. Dyatkin, E. Mamontov, K. M. Cook, and Y. Gogotsi, *Progress in Natural Science-*  
476 *Materials International* **25**(6), 631 (2015).

- 477 30. R. I. Bewley, J. W. Taylor, and S. M. Bennington, *Nuclear Instruments & Methods in*  
478 *Physics Research Section a-Accelerators Spectrometers Detectors and Associated Equipment*  
479 **637**(1), 128 (2011).
- 480 31. F. Mezei, *Physica B-Condensed Matter* **385-86**, 995 (2006).
- 481 32. O. Arnold, J. C. Bilheux, J. M. Borreguero, A. Buts, S. I. Campbell, L. Chapon, M. Doucet,  
482 N. Draper, R. F. Leal, M. A. Gigg, V. E. Lynch, A. Markvardsen, D. J. Mikkelson, R. L.  
483 Mikkelson, R. Miller, K. Palmen, P. Parker, G. Passos, T. G. Perring, P. F. Peterson, S. Ren, M.  
484 A. Reuter, A. T. Savici, J. W. Taylor, R. J. Taylor, R. Tolchenoy, W. Zhou, and J. Zikoysky,  
485 *Nuclear Instruments & Methods in Physics Research Section a-Accelerators Spectrometers*  
486 *Detectors and Associated Equipment* **764**, 156 (2014).
- 487 33. R. T. Azuah, L. R. Kneller, Y. M. Qiu, P. L. W. Tregenna-Piggott, C. M. Brown, J. R. D.  
488 Copley, and R. M. Dimeo, *Journal of Research of the National Institute of Standards and*  
489 *Technology* **114**(6), 341 (2009).
- 490 34. S. Lowell, and J. E. Shields, *Powder surface area and porosity* (Springer Science & Business  
491 Media, **2** (2013).
- 492 35. J. Segalini, B. Daffos, P. L. Taberna, Y. Gogotsi, and P. Simon, *Electrochimica Acta* **55**(25),  
493 7489 (2010).
- 494 36. O. Kimizuka, O. Tanaike, J. Yamashita, T. Hiraoka, D. N. Futaba, K. Hata, K. Machida, S.  
495 Suematsu, K. Tamamitsu, S. Saeki, Y. Yamada, and H. Hatori, *Carbon* **46**(14), 1999 (2008).
- 496 37. R. Mysyk, E. Raymundo-Piñero, and F. Béguin, *Electrochemistry Communications* **11**(3),  
497 554 (2009).
- 498 38. S. Kondrat, P. Wu, R. Qiao, and A. A. Kornyshev, *Nat Mater* **13**(4), 387 (2014).
- 499 39. S. Boukhalfa, D. Gordon, L. He, Y. B. Melnichenko, N. Nitta, A. Magasinski, and G.  
500 Yushin, *ACS Nano* **8**(3), 2495 (2014).
- 501 40. N. C. Osti, A. Cote, E. Mamontov, A. Ramirez-Cuesta, D. J. Wesolowski, and S. O. Diallo,  
502 *Chemical Physics* **465**, 1 (2016).
- 503 41. N. C. Osti, M. Naguib, A. Ostadhossein, Y. Xie, P. R. C. Kent, B. Dyatkin, G. Rother, W. T.  
504 Heller, A. C. T. van Duin, Y. Gogotsi, and E. Mamontov, *Acs Applied Materials & Interfaces*  
505 **8**(14), 8859 (2016).
- 506 42. N. C. Osti, B. Dyatkin, M. W. Thompson, F. Tiet, P. F. Zhang, S. Dai, M. Tyagi, P. T.  
507 Cummings, Y. Gogotsi, D. J. Wesolowski, and E. Mamontov, *Physical Review Materials* **1**(3),  
508 035402 (2017).
- 509 43. M. Bee, *Quasielastic Neutron Scattering: Principles and Applications in Solid State*  
510 *Chemistry, Biology, and Materials Science* (Adam Hilger, Bristol), (1998).
- 511 44. K. S. Cole, and R. H. Cole, *The Journal of Chemical Physics* **9**(4), 341 (1941).
- 512 45. B. Dyatkin, N. C. Osti, A. Gallegos, Y. Zhang, E. Mamontov, P. T. Cummings, J. Wu, and  
513 Y. Gogotsi, *Electrochimica Acta* **283**, 882 (2018).
- 514 46. F. Ferdeghini, Q. Berrod, J. M. Zanotti, P. Judeinstein, V. G. Sakai, O. Czakkel, P. Fouquet,  
515 and D. Constantin, *Nanoscale* **9**(5), 1901 (2017).

516